



Article

Surface Subsidence of Nanchang, China 2015–2021 Retrieved via Multi-Temporal InSAR Based on Long- and Short-Time Baseline Net

Hua Gao ^{1,2}, Luyun Xiong ³, Jiehong Chen ^{1,2,*}, Hui Lin ^{1,2} and Guangcai Feng ⁴

¹ Key Laboratory of Natural Disaster Monitoring, Early Warning and Assessment of Jiangxi Province, School of Geography and Environment, Jiangxi Normal University, Nanchang 330022, China; huagao@jxnu.edu.cn (H.G.); huilin@cuhk.edu.hk (H.L.)

² Key Laboratory of Poyang Lake Wetland and Watershed Research Ministry of Education, Nanchang 330022, China

³ Guangzhou Urban Planning & Design Survey Research Institute, Guangzhou 510060, China; lyxiong@whu.edu.cn

⁴ Key Laboratory of Metallogenic Prediction of Nonferrous Metals and Geological Environment Monitoring, Central South University, Ministry of Education, Changsha 410083, China; fredgps@csu.edu.cn

* Correspondence: chenjiehong@jxnu.edu.cn

Abstract: Urban land subsidence threatens the safety of urban buildings and people's lives. The time series interferometric synthetic aperture radar (InSAR) technology can provide us with large-area, high-resolution, and high-precision ground deformation monitoring. In this study, the time series InSAR technology and the strategy with long- and short-time baseline networking are used to obtain the surface deformation along the line of sight of Nanchang City based on the six-year (from December 2015 to December 2021) Sentinel-1 data. Longer datasets and better baseline strategies allow us to obtain more stable deformation results of Nanchang City than other researchers. The results of surface deformation show that the overall surface of Nanchang City is stable, but there are several obvious subsidence funnels. We carried out a field survey on four areas with significant surface subsidence. We considered that these subsidence areas may be related to soil compaction, building construction, and groundwater extraction. Based on the surface deformation results around the subway line, we analyzed the impact of subway construction on the surface along the line and identified the sections that need to be focused on by the managers to prevent the deformation area from affecting the surrounding buildings and subway line operation safety.

Keywords: surface subsidence; InSAR; geologic hazard; baseline; Nanchang



Citation: Gao, H.; Xiong, L.; Chen, J.; Lin, H.; Feng, G. Surface Subsidence of Nanchang, China 2015–2021 Retrieved via Multi-Temporal InSAR Based on Long- and Short-Time Baseline Net. *Remote Sens.* **2023**, *15*, 3253. <https://doi.org/10.3390/rs15133253>

Academic Editors: Alex Hay-Man Ng, Xiaoqiong Qin, Jie Dong, Xuguo Shi, Joan Ramon Casas Rius, Ling Chang and Jónatas Valença

Received: 16 May 2023
Revised: 16 June 2023
Accepted: 19 June 2023
Published: 24 June 2023



Copyright: © 2023 by the authors. Licensee MDPI, Basel, Switzerland. This article is an open access article distributed under the terms and conditions of the Creative Commons Attribution (CC BY) license (<https://creativecommons.org/licenses/by/4.0/>).

1. Introduction

Urban surface subsidence can damage the structures of roads, bridges, buildings, etc., causing cracks and inclines in buildings. Serious surface subsidence can also cause building and ground collapse [1,2]. These disasters seriously affect the lives and property safety of urban residents. The causes of urban surface deformation mainly fall into two categories: natural factors and human factors. Natural factors include natural changes in groundwater level, fault activities, etc. [3,4]. Human factors include groundwater extraction, subway construction, large-scale surface engineering construction, mineral exploitation, material accumulation, etc. [5–11]. In recent years, people have begun paying increasing amounts of attention to urban surface subsidence and begun to use various means to monitor the surface deformation, discover the area of surface subsidence in advance, and prevent it from inducing hazards. The original method is leveling, which is low in efficiency and high in labor cost; thus, it is not suitable for large-area observations. The Global Navigation Satellite System (GNSS) has greatly improved the efficiency and accuracy of surface deformation monitoring. However, GNSS can only carry out point observation and requires manual

fieldwork. It needs to compromise between the labor cost and the point density and is not suitable for large-scale surface subsidence surveys.

Interferometric synthetic aperture radar (InSAR) is a surface deformation observation technology developed in recent decades [12,13]. It can observe all day and all weather; therefore, it can observe at night and in cloudy or rainy weather. At the same time, the technology has the characteristics of high precision, high spatial resolution, and areal observation, which is very suitable for large-scale ground subsidence surveys. The time series InSAR technology is one of the most important branches of InSAR technology which is based on continuous observation of multi-scene homologous data. This technology can effectively suppress atmospheric and terrain phase residuals. The relative deformation rate accuracy of this technology can reach the millimeter level [1,14]. Permanent scatterers InSAR (PS InSAR) [15] and small baseline subset InSAR (SBAS InSAR) [16] are the most mature and widely used time series InSAR technology. The updated iterative algorithm based on these two types of time series InSAR technology provides a strong technical guarantee for urban surface subsidence monitoring [14,17].

Nanchang is the capital of Jiangxi Province in China, which is located in the central part of China and southwest of Poyang Lake (Figure 1). Nanchang has a permanent population of 6,437,500 (by the end of 2021), with a total area of 7402 km², including 617 km² of the urban area. The city is dotted with lakes. They are Yao Lake, Aixi Lake, Xiang Lake, Qingshan Lake, etc. The urban area is divided into two parts by the Ganjiang River. The east side of the city is a river erosion accumulation plain with flat terrain and many lakes and wetlands. The west side is the tectonic-denuded low land characterized by hills. The terrain gradually rises from River West to the Meiling National Forest Park. The highest elevation of the forest park is 841 m. Mo (2020), Xiong et al. (2021), and Hu et al. (2022) observed the surface deformation of Nanchang City using Sentinel-1 data from 2016 to 2018, 2018 to 2020, and 2019 to 2021, respectively [18–20]. Although the current research has found that there are some subsidence areas in Nanchang, there are some problems such as inconsistent results, short time intervals (no more than 3 years), and lack of observation points in some key areas. In addition, the urban construction of Nanchang has developed rapidly in recent years, and more surface engineering and subway construction projects have started. It is worth studying whether the engineering or subway construction have an impact on the surface and whether hidden dangers are affecting the construction and operation safety in large project areas and the subway line.

In this study, the SBAS InSAR method and ascending orbit dataset of Sentinel-1 for 6 years (from December 2015 to December 2021) are used to obtain the surface deformation in Nanchang City. We carried out a field survey on four areas with significant surface subsidence, and systematically and comprehensively analyzed the subsidence disasters in Nanchang City using the above results. Based on the surface deformation results around the subway line, we analyzed the impact of subway construction on the surface along the line and identified the sections that need to be focused on for reference by the relevant departments to prevent the deformation area from affecting the surrounding buildings and subway line operation safety.

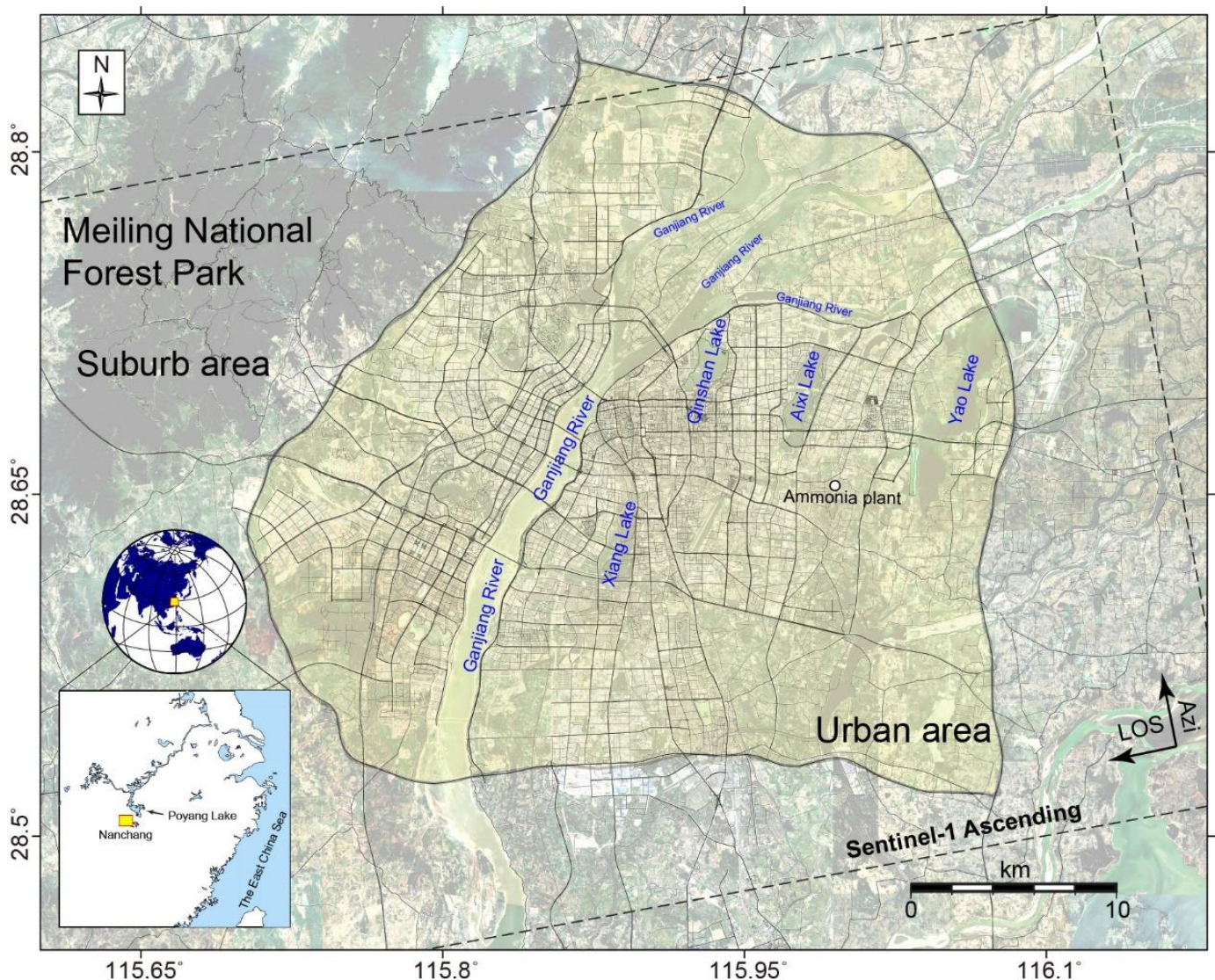


Figure 1. Study area. The yellow background area is the main urban area of Nanchang City. The black line in the main figure is the road network. The black dotted box shows the coverage of Sentinel-1 data used in this study. The inside figure shows the location of Nanchang City.

2. Data and Methods

2.1. Data Coverage

Sentinel-1 is a C-band SAR satellite system developed by the European Space Agency (ESA). The system consists of two satellites Sentinel-1A and B, which were launched in 2014 and 2016, respectively (Sentinel-1B was terminated due to failure on 23 December 2021). The revisit period of the system is 12 days for a single satellite and 6 days for double satellites. The TOPS mode of Sentinel-1 has a spatial resolution of $5 \text{ m} \times 20 \text{ m}$ and a coverage wide of 250 km, which are very suitable for large-area surface deformation monitoring. We obtained the data from the Sentinel-1 satellite (Path 40) over 6 years from 14 December 2015, to 30 December 2021, with a total of 271 scenes. The coverage of data used in this study is shown in the black dotted box in Figure 1.

2.2. Time Series InSAR Analysis Method and the Strategy Adopted in This Study

In this study, the SBAS InSAR method and the GAMMA software are used to obtain the surface deformation of Nanchang City. The SBAS InSAR was proposed by Bernardino et al. [16]. This method constructs interferogram pairs based on the idea of a short baseline

subset to reduce the influence of temporal and spatial incoherence, and to obtain more observation points. At the same time, the small baseline subset can build a more stable baseline network, and obtain a more stable solution when solving the surface deformation rate [21,22]. Because the study area is mainly an urban area, even if the long-time baseline can also have high coherence of interferogram, we adopt the strategy of combining long and short-time baselines to build a baseline network to enhance the stability of the network. In the short-time baseline part, we set the threshold of time span to be less than 48 days, and the threshold of spatial baseline to be less than 150 m. In the long-time baseline part, we set the threshold of time span to be 356–375 days, the threshold of spatial baseline to be less than 25 m, and the impact of the potential biases from the short temporal baseline interferograms can be reduced [23].

We first performed 5:1 (range: azimuth) multi-look processing on single complex images that are well co-registered. The spatial resolution of the image after multi-look is $\sim 25 \text{ m} \times 20 \text{ m}$. We generated interference pairs according to the above strategy. Then, a total of 474 pairs of interferogram were generated, including 324 images of short-time baselines and 150 images of long-time baselines. The baseline network is shown in Figure 2. The shuttle radar topography mission (SRTM DEM) of 30 m resolution is used to remove the topographic phase and flattened phase. Goldstein filtering is applied to interferograms for spatial filtering with a window of 64 and a filter factor of 0.3 [24]. The water area in the interferograms is masked by intensity and coherence. After that, the minimum cost flow method (MCF) is employed for phase unwrapping [25] and the unwrapping interferograms are got. The points are selected according to the amplitude deviation threshold of 0.6 and the coherence of 0.7. The terrain residuals are iteratively removed by the linear regression model (three times) and the points are fine-selected through elevation residuals. Then, temporal (with a box radius of 70 days) and spatial filtering (with a box radius of 50 pixels) are used to reduce the atmospheric phase error. The temporal and spatial filtering results are solved using the linear least squares model [26]. Finally, the line of sight (LOS) surface deformation rate is obtained. Based on the deformation rate results, four areas with obvious subsidence are selected for the field survey. Use mobile phone photography, unmanned aerial vehicle photography, and manual measurement to investigate whether there are road cracks, ground collapse, building cracks, inclination, or collapse in the above key areas, and measure the information such as the crack location, crack width, and inclination angle, etc.

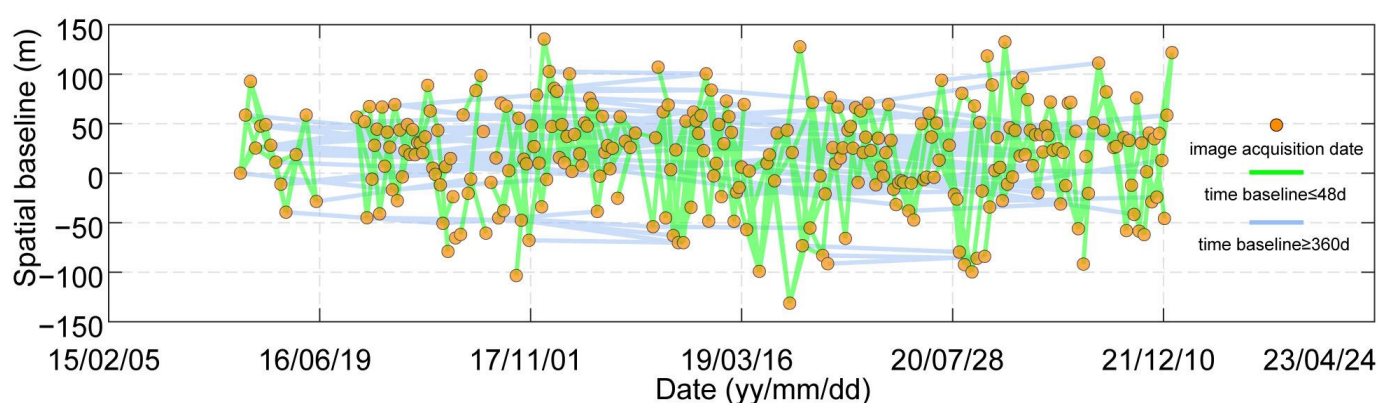


Figure 2. The spatiotemporal baseline net. The yellow dot shows the image acquisition dates. The green line is the short-time (<48 days) baseline and the blue line is the long-time (356–375 days) baseline.

3. Results

The LOS surface deformation of Nanchang City is obtained as shown in Figure 3. Based on the strategy in Section 2, we obtained 4,519,523 measurement points. Except for the fact that there are no observation points in the mountainous area of Meiling National Park, the urban area of Nanchang City is completely covered with high density and uniform distribution of points. The deformation direction obtained using InSAR is the LOS, but the

urban deformation is mainly vertical. In this study, the direction away from the satellite is called subsidence (warm color), and the direction close to the satellite is uplift (cold color). The results show that the surface of Nanchang City is generally stable. The deformation of 98.5% of the observation points is less than 2 mm/year. However, several obvious subsidence funnels were found in Figure 3, all located in and around the main urban areas, and no significant deformation was found in the suburbs. The center deformation rates of these subsidence funnels are more than 3 mm/year, and the maximum is more than 5 mm/year. There are also several concentrated and continuous regional subsidence on the east side of Ganjiang River and the west side of Xiang Lake. We surveyed the four obvious subsidence areas outlined in Figure 3 to verify and compare the deformation results of InSAR with the field investigations. These areas are Xiazhuang Lake (Area A), riverside park (Area B), Shiqi Village (Area C), and the warehouse logistics park (Area D). The spatial resolution of the final deformation field was $\sim 25 \text{ m} \times 20 \text{ m}$. At this resolution, it is enough to observe regional deformation fields and the subsidence of large buildings. However, due to spatial filtering, the deformation of individual observation points may be diluted by the deformation of surrounding points, which undermines the deformation of small buildings. Therefore, in the following text, we focus discussing on the changes and effects of the deformation “field”, without discussing the deformation of small and single buildings.

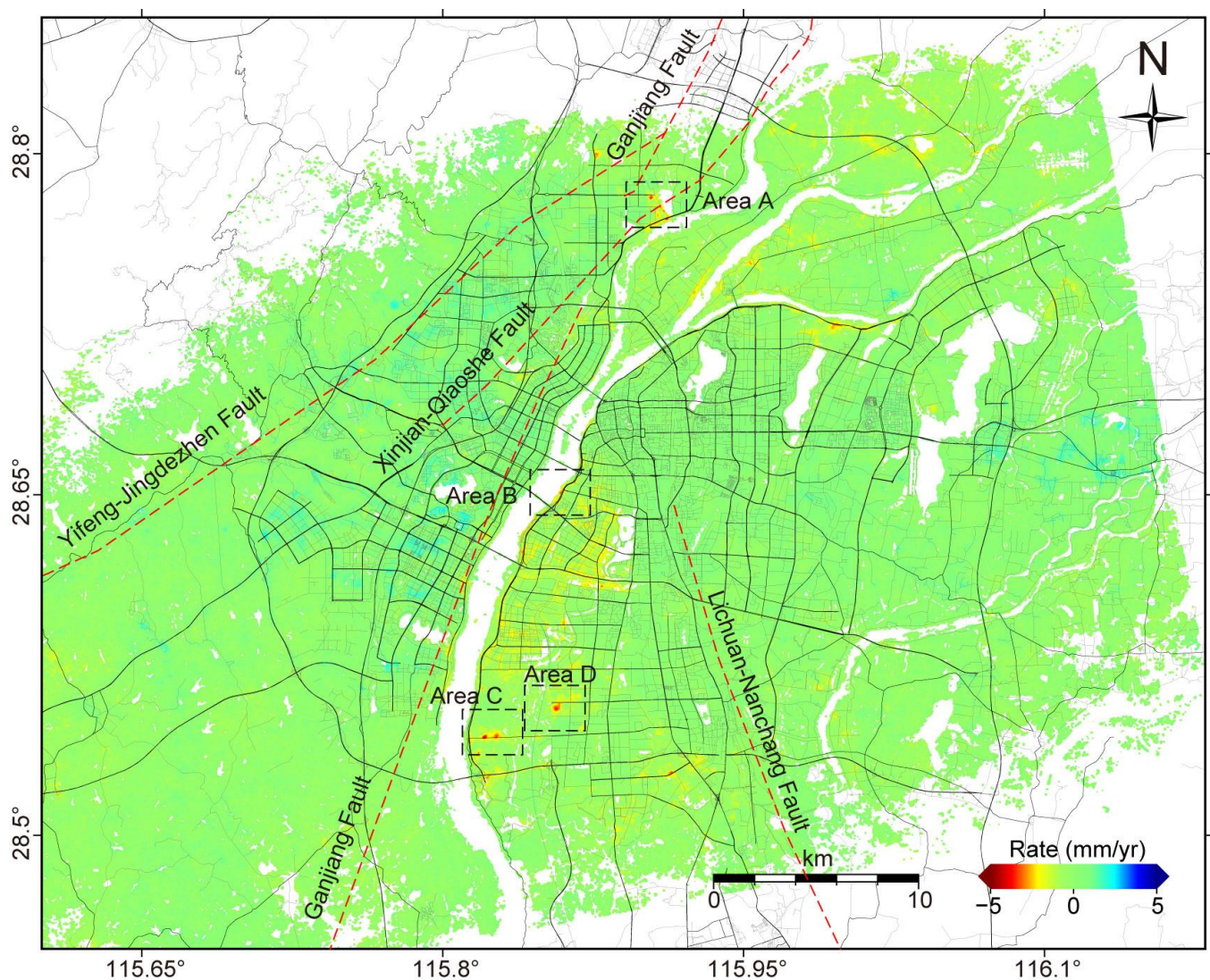


Figure 3. Surface deformation in LOS of Nanchang. The background color in the figure is LOS deformation. The black and gray line is the road. The red dotted line is the fault [27].

Area A (Figure 4a) is located on the west of Xiazhuang Lake. There are three (Figure 4b–d) noteworthy settlements in this region and the regions indicated in Figure 4c,d are the most prominent. These areas have a maximum deformation rate that exceeds 5 mm/year. There is a banded deformation area along the Ganjiang River on the south side of Figure 4a. Through fieldwork, we found that the buildings in Figure 4d are mainly steel structure plants. There are many cracks on the hardened ground near the plant, the width of which reaches 3 cm and the length is tens of meters (Figure 4e). The factory staff reported that the land where the plant was located was a stone stacking area before, and the plant had a history of subsidence and ground cracking for several years after its completion. In Figure 4b, there is an incomplete building. The deformation area mainly includes bare land, surrounding roads, and walls near incomplete buildings. We found many cracks in the surrounding walls, with a crack width of ~2 cm. We also found collapsed ground and inclined walls around. The area shown in Figure 4c is located between the north bank of the Ganjiang River and a viaduct along the river. There is a newly built wharf near the river bank. However, the steel structure building in Figure 4c has not started construction during our observation period, and it is originally bare land. The area marked in Figure 4f is the sluice gate from Xiazhuang Lake to Ganjiang River, where the subsidence is obvious. After the ground is hardened and the building is completed, an obvious settlement can still be observed in Figure 4f. Hardened ground inclination and cracks (more than 2 cm wide) caused by subsidence near the gate area can be observed. The linear deformation area along the Ganjiang River is located in the bare land in the south of the viaduct. In the fieldwork, it is not found that the viaduct is affected.

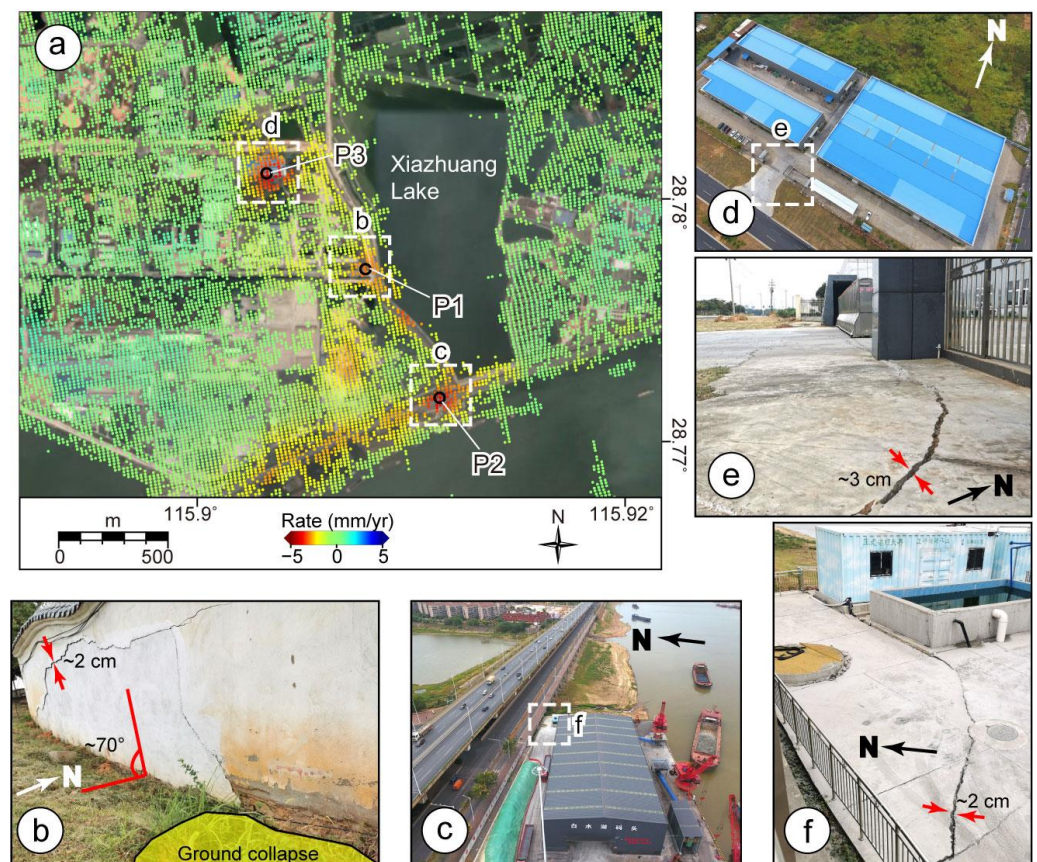


Figure 4. LOS surface deformation and fieldwork results in the west of Xiazhuang Lake (Area A). (a) LOS surface deformation of Area A. (b–f) the fieldwork results of Area A.

Area B is located in a riverside park, which was built around 2016. The original site is bare land formed due to river erosion accumulation. There are no other artificial buildings

in the subsidence area except for two plastic basketball courts and a single-story building. According to the fieldwork, we found that there are dense cracks in the hardened pavement in the area with large subsidence (Figure 5a), and some cracks can be 2 cm wide. However, the density of pavement cracks without obvious deformation areas is relatively low.

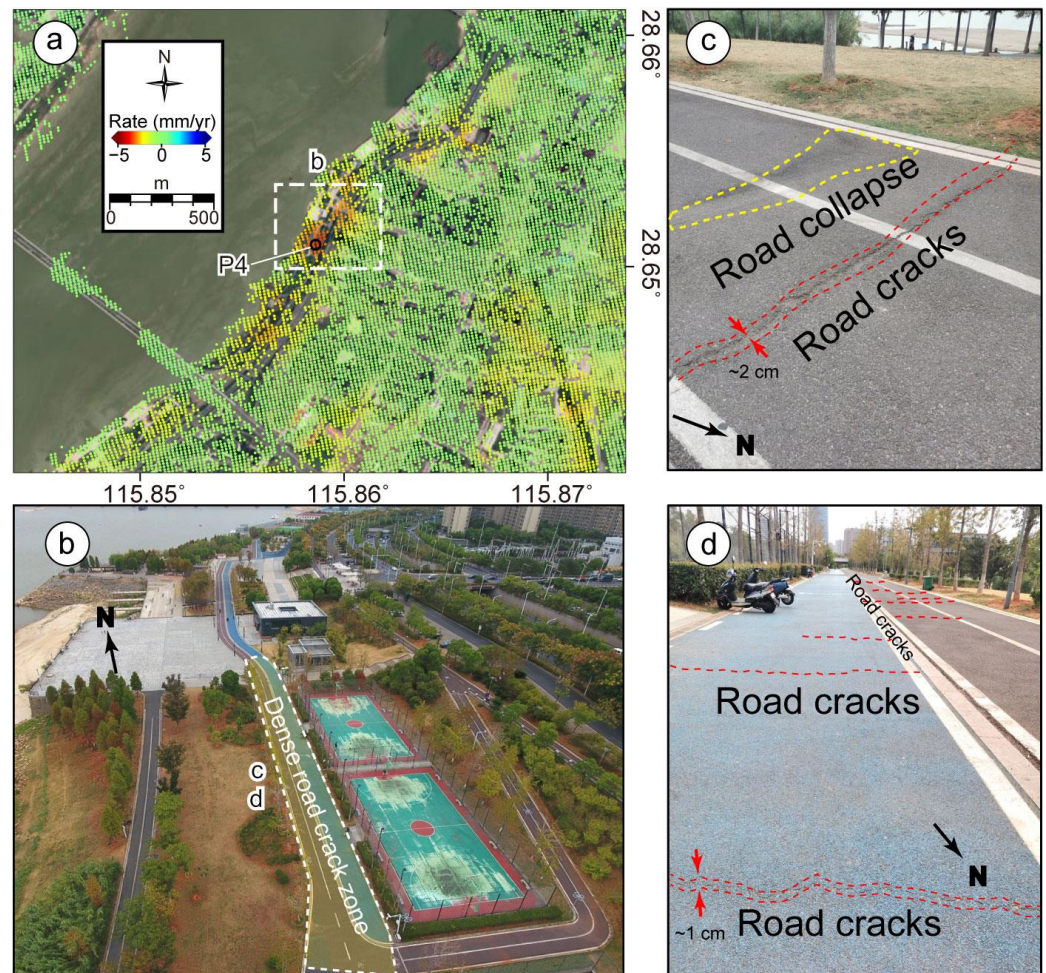


Figure 5. LOS surface deformation and fieldwork results in a riverside park (Area B). (a) LOS surface deformation of Area B. (b–d) the fieldwork results of Area B.

The main subsidence of Area C (Figure 6a) is located in a transitional resettlement community in the Shiqi village, which is in the south of the city. The resettlement community can be divided into C1, C2, and C3 according to the construction time (Figure 6b,c). The resettlement community consists of dozens of simple single-story bungalows, with the top covered with stone and iron tiles. From the deformation results, it can be found that the deformation rate of C1, which was the earliest constructed area, is the lowest (<2 mm/year), followed by C2 (~3 mm/year); the largest deformation is the recently constructed C3 area, and the deformation rate of the subsidence center exceeds 4 mm/year. According to the fieldwork, no obvious cracks or inclinations are found in the building; however, there are many cracks in the surrounding walls of the building area, the maximum width of which is more than 4 cm. In some sections, there are large area cracks in the walls and ground collapse. In addition, a railway line is adjacent to the deformation area. The surface deformation may affect the safety of railway operations.

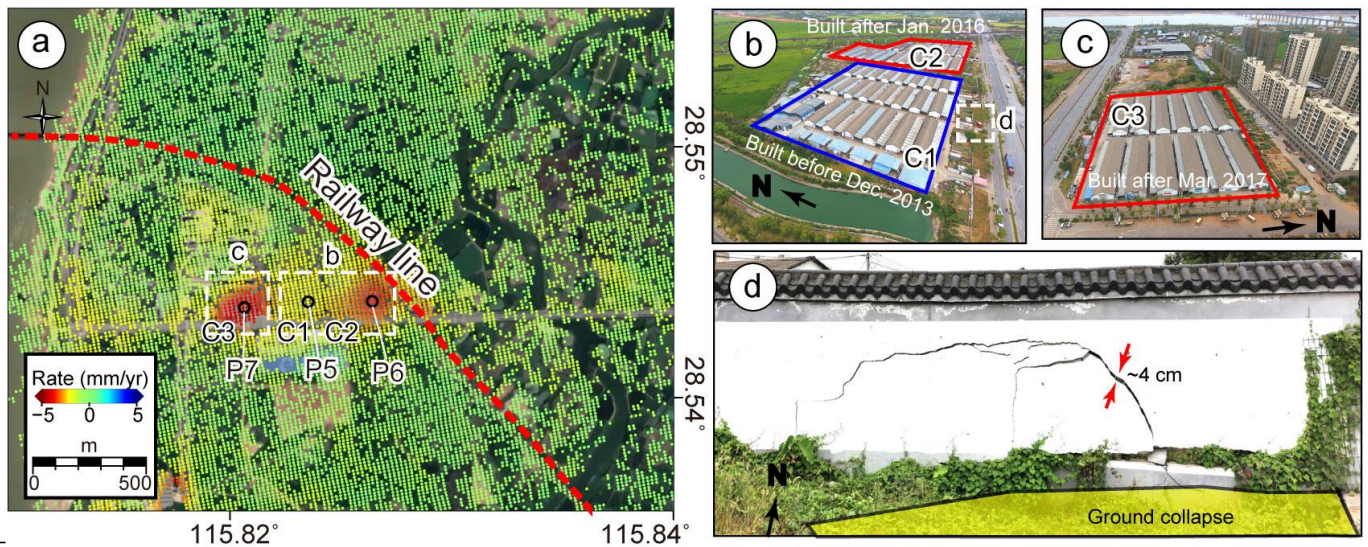


Figure 6. LOS surface deformation and fieldwork results of Shiqi Village resettlement community (Area C). (a) LOS surface deformation of Area C. (b–d) the fieldwork results of Area C.

Area D is located in a logistics warehousing park (Figure 7). The buildings in this area are mainly steel structure plants, and the top is mostly covered with iron tiles. During the fieldwork, we found no obvious ground cracks, nor obvious wall deformation and cracking.

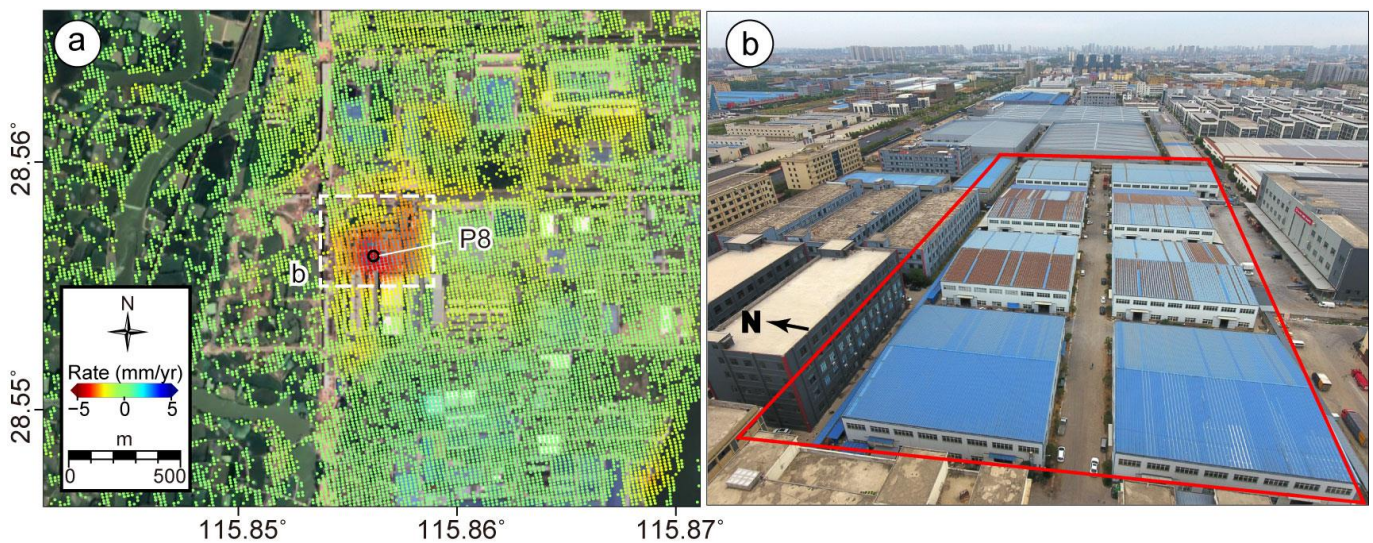


Figure 7. LOS surface deformation and fieldwork results of the warehouse logistics park (Area D). (a) LOS surface deformation of Area D. (b) the fieldwork results of Area D.

4. Discussion

4.1. Precision Checking

Due to the stable deformation in Nanchang City and no trend deformation being found, the standard deviation of the deformation rate at all observation points can be used to measure the precision of deformation results [28,29]. The methods are as follows:

$$\sigma_v = \sqrt{\frac{\sum_{j=1}^m (V_j)^2}{m}} \quad (1)$$

where σ_v is the standard deviation of all rate values. m is the number of observation points. V_j is the deformation rate of point j . Due to the small deformation area and magnitude in this case, no masking treatment was performed.

The distribution of all observation deformation rates is shown in Figure 8a. The result shows that the deformation in Nanchang City is an almost normal distribution. The standard deviation of all deformation values is 0.52 mm/year, which indicates that our observation results have high precision.

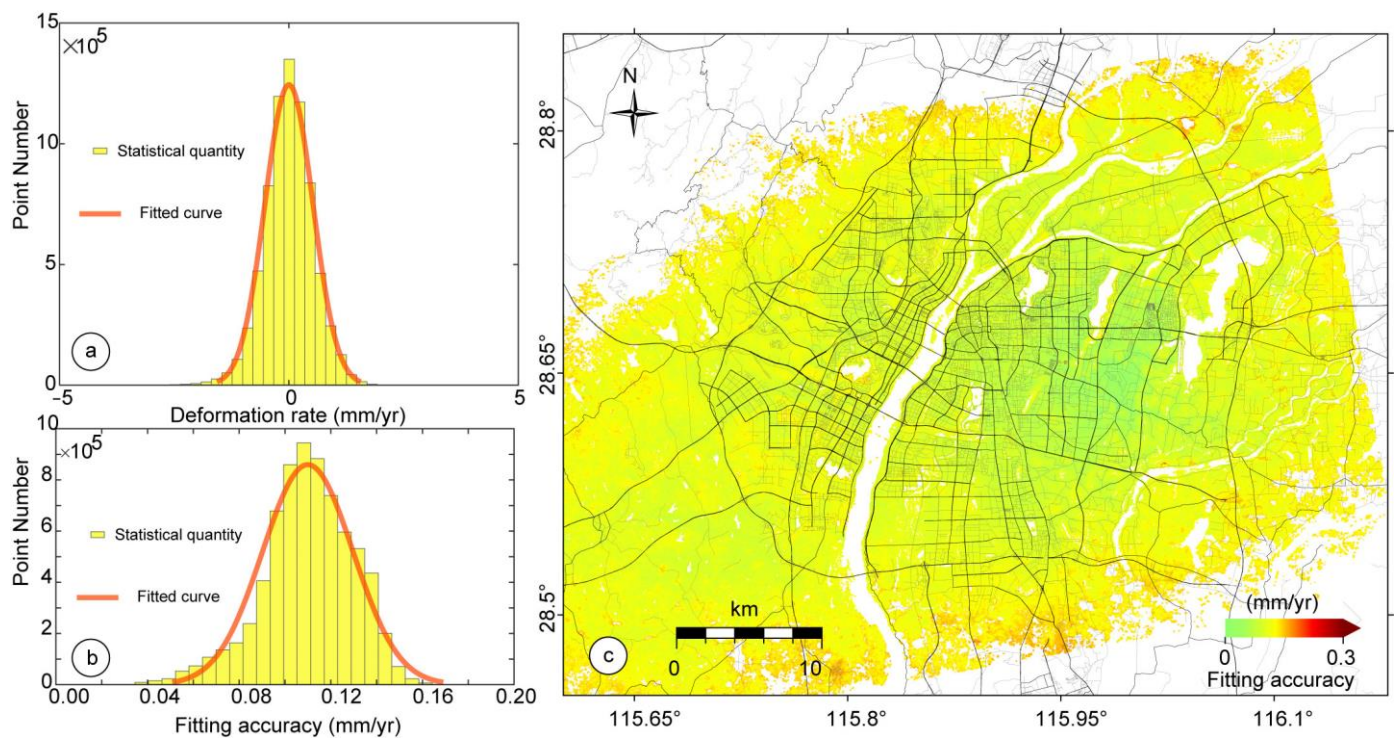


Figure 8. Precision and statistical chart of LOS deformation. (a) The distribution of all observation deformation rates. (b) The distribution of fitting accuracy. (c) The figure of fitting accuracy.

We also evaluate the precision of the LOS deformation rate in Nanchang according to the fitting standard deviation of the linear rate. The solution formula is as follows:

$$\sigma_i = \sqrt{\frac{\sum_{k=1}^n (def_{fit,k} - def_{inf,k})^2}{n}} \quad (2)$$

where σ_i is the rate standard deviation of point i . n is the number of interferograms involved in the calculation of the deformation rate. $def_{inf,k}$ is the deformation of point i obtained from the k_{th} interferograms, $def_{fit,k}$ is the deformation of point i fitted by the deformation rate. We solved the standard deviation of each observation point according to the above formula, and the result is shown in Figure 8b,c. The statistical analysis of the standard deviation of all points (Figure 8b) shows that the overall precision of the deformation rate map is between 0.064 and 0.144 mm/year (95% confidence interval). The precision of urban areas is generally better than that of suburban areas. The maximum value is 0.186 mm/year, which is located on the west side of the Ganjiang River.

Indeed, the true deformation rate error cannot be reflected by simply using the above two methods. Unfortunately, we have not been able to obtain effective GNSS or leveling deformation data for comparison in order to make more accurate estimates. However, the standard deviation of deformation and fitting accuracy results in this paper can reflect

the stability of the deformation time series and the accuracy of the deformation rate to a certain extent.

4.2. Cause Analysis of the Deformation in Nanchang

There are four faults in the urban area of Nanchang, including the Lichuan–Nanchang fault, Yifeng–Jingdezhen fault, Ganjiang fault, and Xinjian–Qiaoshe fault. The first fault is located on the east bank of the Ganjiang River, and the others are located on the east bank [27]. These faults have not been activated since 1900 [30]. We have not found the surface deformation caused by these faults in the Nanchang urban area (Figure 3).

Nanchang began to use machinery to exploit groundwater for chemical and steel industries in the 1950s. In the mid-1970s, the amount of groundwater exploitation reached its peak and was stable until 2007. Three groundwater downcomer centers, namely Jiangfang, Hongdu, and the ammonia plant, were formed. Zou et al. speculated that the ammonia plant would still be the funnel center in 2020 by using the numerical simulation of the groundwater system [31]. However, according to our deformation results and Mo's study (2020), no significant subsidence was found in this area [18]. This may be related to the fact that the government has strengthened the planning and management of groundwater exploitation and the change in groundwater level is stable.

4.2.1. Subsidence of Building

The deformation area in Figure 4d may come from soil compaction. This area was once a rock dump before the construction of buildings, and the existing steel structure buildings were constructed after filling based on the dump. We speculate that the subsidence in this area is related to the natural subsidence of soil accumulation and the shallow foundation of steel structure buildings. The area of packed loess is characterized by a weak structure and loose arrangement of soil grains [32]. From the time series curve of the center of the subsidence funnel (Figure 9c), the subsidence rate in this area is relatively stable, with an average LOS subsidence rate of 3.4 mm/year.

In addition, industrial or domestic water utilization may also be the cause of subsidence. Some factories or residential areas use methods such as drilling wells and pumping water to obtain production and domestic water. Groundwater exploitation can have an impact on the pore structure and stress state of underground rock masses, leading to pore elastic effects. Extracting groundwater will lower the groundwater level, leading to a decrease in pore water pressure in the underground rock mass, a decrease in water molecules in the pores, and a decrease in the volume of the pores. Finally, these lead to the elastic modulus and Poisson's ratio change, thus causing the displacement of underground rock or soil, ultimately transmitting to the surface [33,34]. From the deformation results, there is a high spatial correlation between several obvious subsidence areas (Figures 4d, 6 and 7) and the location of residential areas or industrial plants.

The houses shown in Figure 6b,c are simple and single-story bungalows. Before the construction of resettlement housing, the area was composed of several ponds and bare land. The house is built after filling and leveling the area. We speculate that the subsidence in this area is also mainly related to the natural subsidence of soil accumulation and the shallow foundation. We find that the average subsidence rates of P5, P6, and P7 are 2.0 mm/year, 3.4 mm/year, and 4 mm/year, respectively (Figure 9), which increase with the construction time sequence. This is consistent with the characteristics of soil compaction deformation decreasing with time [35]. However, the time series curve of the subsidence centers in these three regions shows (Figure 9e–g) that their subsidence rates show an increasing trend at the end of 2019. In particular, the C1 area was stable before 2019, but it began to settle slowly at the end of 2019 (Figure 9e). We infer that it may relate to the increase in residential water consumption.

The main deformation of Area D is almost completely covered by the steel structure plant. The deformation at P8 in Figure 9h shows that the area is linearly deformed at a rate of 3.5 mm/year. We have not found any signs of surface subsidence such as cracks

or inclines in Area D; therefore, we infer that this deformation is related to the natural deformation of steel structural materials on the top of the building.

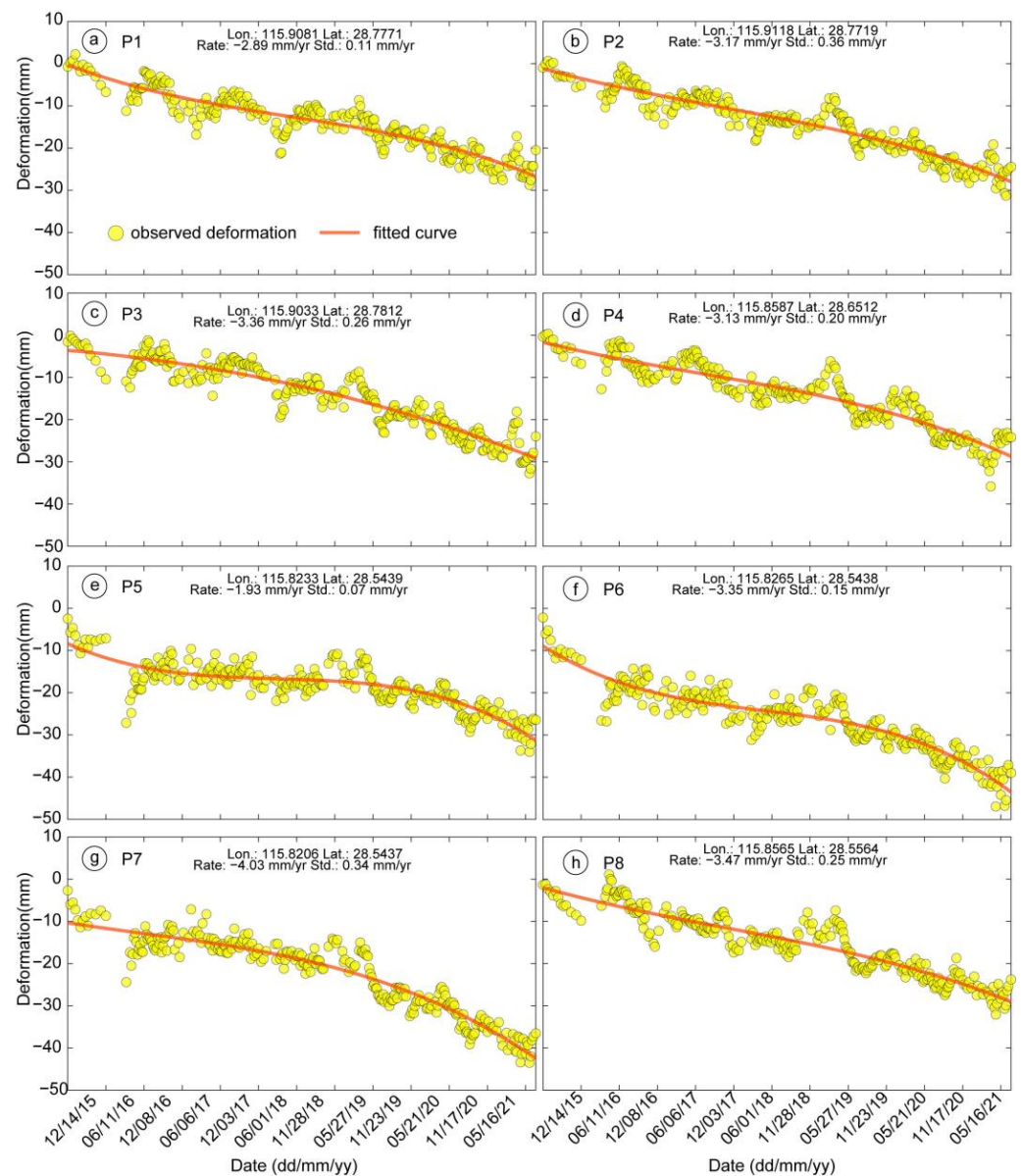


Figure 9. Time series deformation curve of main subsidence area. The time series is the average of observation points within a radius of 50 m. (a–h) Time series deformation of points P1–P8.

4.2.2. Subsidence of Bare Land

We speculate that the subsidence of the areas shown in Figures 4b,c and 5b are natural deformation of bare land accumulation. There are no artificial buildings in these areas during our observation period; however, these areas are all located at the edge of lakes and rivers. The soil in these areas is relatively soft and slowly deforms with time after land leveling. The subsidence rates in these regions are also small and stable (Figure 9a,b,d). The center subsidence rates of Figure 4b,c, and 5b (P1, P2, P4) are 2.9 mm/year, 3.2 mm/year, and 3.1 mm/year, respectively. The subsidence magnitude in Figure 4c of Area A is the largest, which may be related to that the area is located in the drainage outlet from the lake to the river. At present, hardened pavement and buildings have been built in this area, but obvious cracks and slopes have been found in the hardened pavement during field

investigation (Figure 4f), and the subsidence in this area may affect the safety of buildings in this area.

4.2.3. Subsidence Related to Subway Line

We have extracted deformation points within a radius of 250 m along the subway line to observe the ground subsidence (Figure 10). The results show that the deformation in most areas of the completed lines is within 1 mm/year, and a small regional deformation of about 2 mm/year exists in a few sections such as riverside, lakeside, and park sections. In the north extension section of Line 1 (planning), there is an obvious subsidence funnel, where the central velocity of the funnel is 2.9 mm/year (Figure 10b, S1), and its deformation curve is shown in Figure 11a. This section of the subway line has not been constructed within the observation period in this study; therefore, the deformation here is not caused by subway construction. The subsidence funnel here may bring hidden danger to the planned subway construction, which deserves the attention of relevant departments of subway construction. In addition to the obvious deformation shown in Figure 10b, there are also a few small amounts of deformation (<2 mm/year) areas along the river as shown in Figure 10e–g (S2, S3, S4). After comparing the deformation results to historical optical images, we found that the deformation in these areas may be caused by the natural compaction of stacked soil. The areas shown in Figure 10c,d,h close to the subway line have a small amount of local deformation. These areas are close to rivers, lakes, and farmland. The deformation in these areas may be caused by the natural subsidence of soft soil or the error caused by water vapor. The deformation time series in Figure 11d experienced significant abnormal changes after July 2021, with the deformation suddenly transitioning from continuous subsidence to uplift. After comparing historical optical images, we found that there were significant changes in the surface buildings at the location of S4 between June and July 2021, which caused anomalies in the deformation time series.

4.2.4. Impact of Errors

Although the strategy of combining long and short-time baselines and images covered for a long time has greatly improved the stability of deformation rate results, the influence of temporal decoherence and atmospheric error cannot be completely avoided. The most obvious error is the phase jump between June 2016 and September 2016. Due to the lack of images in this period, there are errors in the rate and time series solution. In addition, there are small regional error components near water areas. We have fully optimized the baseline net and reduced the impact of the terrain residuals and atmospheric phase on the results through temporal and spatial filtering; however, it cannot be completely removed. This is finally reflected in the deformation rate field. However, on the whole, the error of our results is small, the internal fitting accuracy is within 0.2 mm/year, and the distribution of the fitting error of the observation points conforms to the normal distribution (Figure 8).

As mentioned above, the true deformation rate error cannot be reflected solely by the standard deviation of the deformation rate and the internal fitting accuracy. Unfortunately, we have not been able to obtain effective GNSS or leveling deformation data for comparison in order to make more appropriate precision estimates. However, our estimation results can reflect the stability of the deformation time series and the accuracy of the deformation rate to a certain extent. The magnitude of error of our results can be ignored in the tasks of extracting regional ground deformation; however, strategies can be modified to further reduce the impact of error when monitoring specific small areas or building deformation.

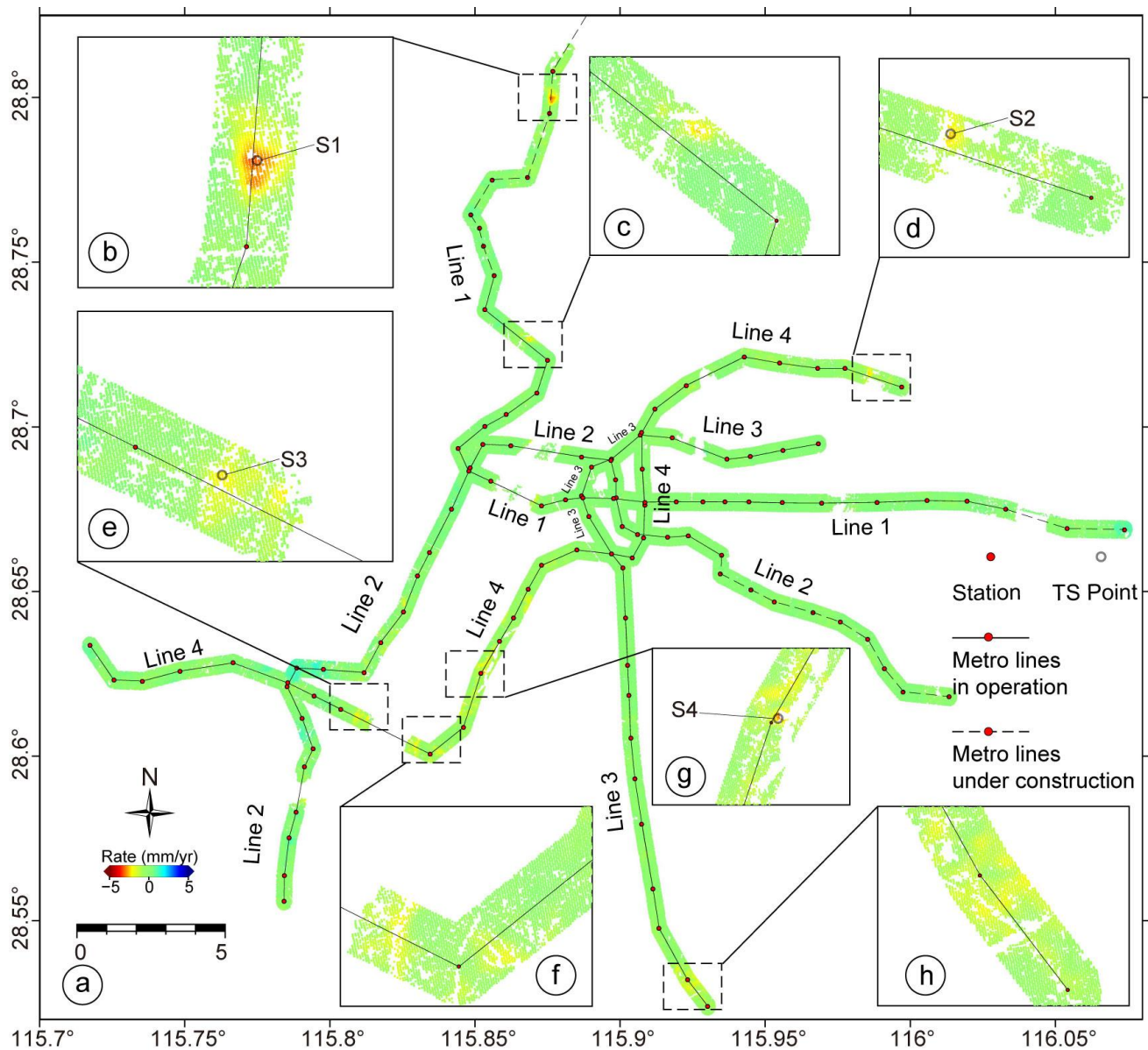


Figure 10. LOS deformation along the Metro. (a) Global LOS deformation along the Metro (b–h) Enlarged view of obvious deformation areas along the subway line.

4.3. The Difference between our Results and the Existing Results

4.3.1. Time and Space Coverage

To extract the deformation field, we used six-year Sentinel-1 data and the network construction strategy of combining long and short-time baselines, which led our observation results to cover all urban areas and most suburbs of Nanchang City and obtain a sufficient number of observation points. Since we have adopted a longer time series period, we can obtain a longer time surface change information of Nanchang City from the results, and the information obtained is more reliable. For example, there are only a few observation points in the southwest, southeast and northeast regions from the results of Xiong et al. (2021). The results of Mo (2020) also have serious gaps in the northeast and southwest [18,19].

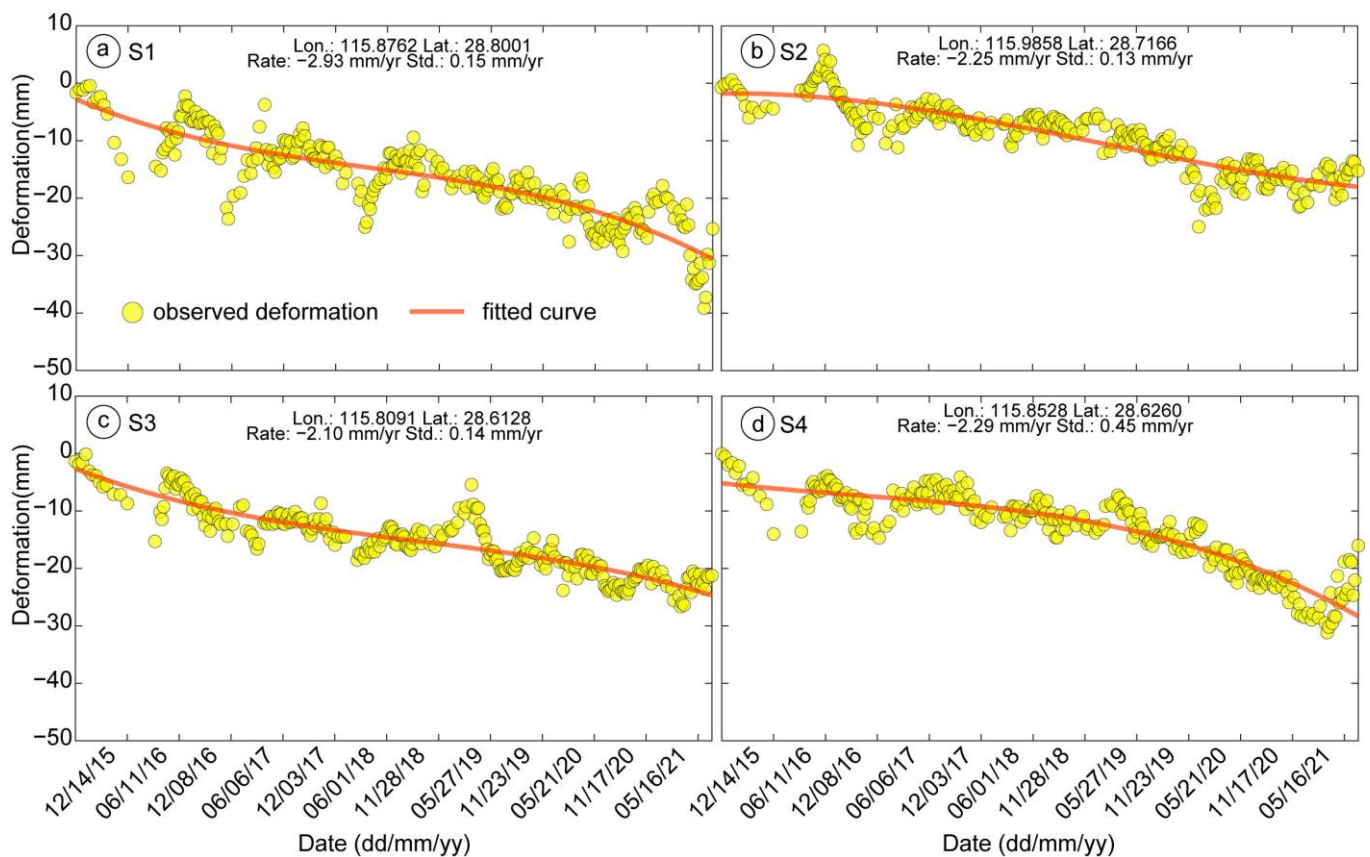


Figure 11. Time series deformation curve of subsidence area along the subway lines. The time series is the average of observation points within a radius of 50 m. Time series deformation of points S1–S4.

4.3.2. Stability and Accuracy of the Results

We have used spatial filtering to reduce the impact of the noise phase, which makes our results stable and accurate for regional deformation. Compared with the existing results, our deformation results have less noise and more stable deformation curves. In addition, the long time series can effectively weaken the atmospheric phase jitter, which makes our results more reliable than those of Xiong et al. (2021) and Mo (2020) [18,19]. From their results, significant noise points and abnormal deformation can be found, and the overall deformation is relatively large.

4.3.3. Observed Subsidence Area

We have found subsidence areas shown in the west of Xiaozhuang Lake (Area A), the riverside park (Area B), the Shiqi Village (Area C), the warehouse logistics park (Area D), and regional subsidence, which is consistent with the results of Xiong et al. (2021). However, in Area C, we observed more obvious subsidence, and Xiong et al. (2021) failed to obtain effective observation points. In addition, we observed denser points in Area A and Area D than Xiong et al. reported (2021) [19]. It is inconvenient to compare the results with those of Hu et al. (2022) for few observation points are obtained and trend phases maybe have not been removed completely in Hu et al.'s work (2022) [20]. However, from the time series of some points provided, we can find that the stability of our results has been improved compared with their results.

5. Conclusions

In this study, the SBAS InSAR technology and the baseline networking strategy with long- and short-time baseline are used to obtain the LOS surface deformation of Nanchang City based on six-year Sentinel-1 data. The results of surface deformation and fieldwork

show that the overall surface of Nanchang City is stable; however, there are several obvious subsidence funnels. Fortunately, these areas are mainly bare land, bungalows, and factory buildings without high-rise buildings. During the field investigation, we only observed the damage of hardened ground and low walls, and no obvious signs of other building damage were found. These subsidence areas may be related to soil compaction, building construction, and groundwater extraction. One obvious subsidence funnel and six weak subsidence areas have been found along the subway, which may endanger the safety of subway construction and operation and deserve the attention of the relevant departments.

Author Contributions: Methodology, H.G. and G.F.; Investigation, H.G. and J.C.; Writing—original draft, H.G.; Writing—review & editing, L.X., J.C., H.L. and G.F. All authors have read and agreed to the published version of the manuscript.

Funding: This work was supported by the Science and Technology Research Project of the Jiangxi Provincial Department of Education (Grant No. GJJ2200374), the Open Fund of Key Laboratory of Natural Disaster Monitoring, Early Warning and Assessment of Jiangxi Provincial (Grant No. JXZRZH202301).

Data Availability Statement: The Sentinel-1 images are from the Copernicus Open Access Hub (<https://scihub.copernicus.eu/>, accessed on 1 March 2023) of the European Space Agency (ESA). The seismic information was provided by U. S. Geological Survey (USGS, <https://earthquake.usgs.gov/earthquakes/search/>, accessed on 1 March 2023) and The Global Centroid-Moment-Tensor Project (GCMT, <http://www.globalcmt.org>, accessed on 1 March 2023).

Acknowledgments: Some of the images in this study were drawn using the Generic Mapping Tools (GMT) which is open-source software. The fieldwork was assisted by Shan He.

Conflicts of Interest: The authors declare no conflict of interest.

References

1. Liao, M.S.; Wang, T. *Time Series InSAR Technology and Application*; Science Press: Beijing, China, 2014.
2. Raspini, F.; Caleca, F.; Del Soldato, M.; Festa, D.; Confuorto, P.; Bianchini, S. Review of satellite radar interferometry for subsidence analysis. *Earth-Sci. Rev.* **2022**, *235*, 104239. [[CrossRef](#)]
3. Lu, Z.; Danskin, W.R. InSAR analysis of natural recharge to define structure of a ground-water basin, San Bernardino, California. *Geophys. Res. Lett.* **2001**, *28*, 2661–2664. [[CrossRef](#)]
4. Tong, X.; Sandwell, D.T.; Smith-Konter, B. High-resolution interseismic velocity data along the San Andreas Fault from GPS and InSAR. *J. Geophys. Res. Solid Earth* **2013**, *118*, 369–389. [[CrossRef](#)]
5. Perissin, D.; Wang, Z.; Lin, H. Shanghai subway tunnels and highways monitoring through Cosmo-SkyMed persistent scatterers. *ISPRS J. Photogramm. Remote Sens.* **2012**, *73*, 58–67. [[CrossRef](#)]
6. Chaussard, E.; Amelung, F.; Abidin, H.; Hong, S.H. Sinking cities in Indonesia: ALOS PALSAR detects rapid subsidence due to groundwater and gas extraction. *Remote Sens. Environ.* **2013**, *128*, 150–161. [[CrossRef](#)]
7. Chaussard, E.; Wdowinski, S.; Cabral-Cano, E.; Amelung, F. Land subsidence in central Mexico detected by ALOS InSAR time-series. *Remote Sens. Environ.* **2014**, *140*, 94–106. [[CrossRef](#)]
8. Yang, C.S.; Zhang, Q.; Zhao, C.Y.; Wang, Q.L.; Ji, L.Y. Monitoring land subsidence and fault deformation using the small baseline subset InSAR technique: A case study in the Datong Basin, China. *J. Geodyn.* **2014**, *75*, 34–40. [[CrossRef](#)]
9. Xu, B.; Feng, G.C.; Li, Z.W.; Wang, Q.J.; Wang, C.C.; Xie, R.G. Coastal subsidence monitoring associated with land reclamation using the point target based SBAS-InSAR method: A case study of Shenzhen, China. *Remote Sens.* **2016**, *8*, 652. [[CrossRef](#)]
10. Guzy, A.; Malinowska, A.A. State of the art and recent advancements in the modelling of land subsidence induced by groundwater withdrawal. *Water* **2020**, *12*, 2051. [[CrossRef](#)]
11. Yang, Z.F.; Li, Z.W.; Zhu, J.J.; Wang, Y.D.; Wu, L.X. Use of SAR/InSAR in mining deformation monitoring, parameter inversion, and forward predictions: A review. *IEEE Geosci. Remote Sens. Mag.* **2020**, *8*, 71–90. [[CrossRef](#)]
12. Hooper, A.; Bekaert, D.; Spaans, K.; Arikan, M. Recent advances in SAR interferometry time series analysis for measuring crustal deformation. *Tectonophysics* **2012**, *514*, 1–13. [[CrossRef](#)]
13. Biggs, J.; Wright, T.J. How satellite InSAR has grown from opportunistic science to routine monitoring over the last decade. *Nat. Commun.* **2020**, *11*, 3863. [[CrossRef](#)] [[PubMed](#)]
14. Osmanoğlu, B.; Sunar, F.; Wdowinski, S.; Cabral-Cano, E. Time series analysis of InSAR data: Methods and trends. *ISPRS J. Photogramm. Remote Sens.* **2016**, *115*, 90–102. [[CrossRef](#)]
15. Ferretti, A.; Prati, C.; Rocca, F. Nonlinear subsidence rate estimation using permanent scatterers in differential SAR interferometry. *IEEE Trans. Geosci. Remote Sens.* **2000**, *38*, 2202–2212. [[CrossRef](#)]

16. Berardino, P.; Fornaro, G.; Lanari, R.; Sansosti, E. A new algorithm for surface deformation monitoring based on small baseline differential SAR interferograms. *IEEE Trans. Geosci. Remote Sens.* **2002**, *40*, 2375–2383. [CrossRef]
17. Zhang, Y.J.; Heresh, F.; Falk, A. Small baseline InSAR time series analysis: Unwrapping error correction and noise reduction. *Comput. Geosci.* **2019**, *133*, 104331. [CrossRef]
18. Mo, Y. Land subsidence monitoring and risk assessment based on time series InSAR technology in Nanchang City. Master's Thesis, East China University of Technology, Nanchang, China, 2020. (In Chinese). Available online: <http://www.cnki.net/> (accessed on 1 March 2023).
19. Xiong, J.C.; Xiao, R.Y.; He, X.F. Land surface deformation in Nanchang, China 2018–2020 revealed by multi-temporal InSAR. *Nat. Hazard. Res.* **2021**, *1*, 187–195. [CrossRef]
20. Hu, B.; Chen, B.X.; Na, J.; Yao, J.Q.; Zhang, Z.M.; Du, X.F. Urban surface deformation management: Assessing dangerous subsidence areas through regional surface deformation, natural factors, and human activities. *Sustainability* **2022**, *14*, 10487. [CrossRef]
21. Li, S.W.; Xu, W.B.; Li, Z.W. Review of the SBAS InSAR time-series algorithms, applications, and challenges. *Geod. Geodyn.* **2022**, *12*, 114–126. [CrossRef]
22. Gao, H.; Liao, M.S.; Liang, X.; Feng, G.C.; Wang, G.H. Coseismic and Postseismic fault kinematics of the July 22, 2020, Nima (Tibet) Ms6.6 earthquake: Implications of the forming mechanism of the active N-S-trending grabens in Qiangtang, Tibet. *Tectonics* **2022**, *41*, e2021TC006949. [CrossRef]
23. Ou, Q.; Daout, S.; Weiss, J.R.; Shen, L.; Lazecký, M.; Wright, T.J.; Parsons, B.E. Large-scale interseismic strain mapping of the NE Tibetan Plateau from Sentinel-1 interferometry. *J. Geophys. Res. Solid Earth* **2022**, *127*, e2022JB024176. [CrossRef]
24. Goldstein, R.M.; Werner, C.L. Radar interferogram filtering for geophysical applications. *Geophys. Res. Lett.* **1998**, *25*, 4035–4038. [CrossRef]
25. Costantini, M. A novel phase unwrapping method based on network programming. *IEEE Trans. Geosci. Remote Sens.* **1998**, *36*, 813–821. [CrossRef]
26. Wegmuller, U.; Werner, C. Retrieval of vegetation parameters with SAR interferometry. *IEEE Trans. Geosci. Remote Sens.* **1997**, *35*, 18–24. [CrossRef]
27. Institute of Geology, China Seismological Bureau. China Seismic Fault Information System. (In Chinese). Available online: <https://data.activetectonics.cn/arcportal/apps/webappviewer/index.html?id=684737e8849c4170bbca14447608c451> (accessed on 1 March 2023).
28. Dong, S.; Samsonov, S.; Yin, H.; Ye, S.; Cao, Y. Time-series analysis of subsidence associated with rapid urbanization in Shanghai, China measured with SBAS InSAR method. *Environ. Earth Sci.* **2014**, *72*, 677–691. [CrossRef]
29. Luo, H.; Wang, T.; Wei, S.; Liao, M.S.; Gong, J.Y. Deriving centimeter-level coseismic deformation and fault geometries of small-to-moderate earthquakes from time-series Sentinel-1 SAR images. *Front. Earth Sci.* **2021**, *9*, 636398. [CrossRef]
30. U.S. Geological Survey. Earthquake Lists, Maps, and Statistics. Available online: <https://earthquake.usgs.gov/earthquakes/search/> (accessed on 1 March 2023).
31. Zou, Y.Q.; Lan, Y.Y.; Zhou, W.B.; Zhong, M.S. Numerical simulations of groundwater systems in Nanchang city. *J. Nanchang Univ. (Nat. Sci.)* **2012**, *36*, 507–510.
32. He, Y.; Chen, Y.; Wang, W.; Yan, H.; Zhang, L.; Liu, T. TS-InSAR analysis for monitoring ground deformation in Lanzhou New District, the loess Plateau of China, from 2017 to 2019. *Adv. Space Res.* **2021**, *67*, 1267–1283. [CrossRef]
33. Zhou, L.; Guo, J.M.; Hu, J.Y.; Li, J.W.; Xu, Y.F.; Pan, Y.J.; Shi, M. Wuhan surface subsidence analysis in 2015–2016 based on Sentinel-1A data by SBAS-InSAR. *Remote Sens.* **2017**, *9*, 982. [CrossRef]
34. Dal Zilio, L.; Hegyi, B.; Behr, W.; Gerya, T. Hydro-mechanical earthquake cycles in a poro-visco-elasto-plastic fluid-bearing fault structure. *Tectonophysics* **2022**, *838*, 229516. [CrossRef]
35. Root, A.W. California Experience in construction of highways across Marsh Deposits. *Highw. Res. Board Bull.* **1958**, *173*, 46–64. Available online: <http://onlinepubs.trb.org/Onlinepubs/hrbulletin/173/173-003.pdf> (accessed on 1 March 2023).

Disclaimer/Publisher's Note: The statements, opinions and data contained in all publications are solely those of the individual author(s) and contributor(s) and not of MDPI and/or the editor(s). MDPI and/or the editor(s) disclaim responsibility for any injury to people or property resulting from any ideas, methods, instructions or products referred to in the content.